Research Article

Effect of Gd^{3+} doping on structural and photocatalytic properties of ZnO obtained by facile microwave-hydrothermal method

Juliane Z. Marinho[1] · **Leonardo F. de Paula**[1] · **Elson Longo**[2] · **Antonio O. T. Patrocinio**[1] · **Renata C. Lima**[1]

Abstract

Gd^{3+}-doped ZnO nanoparticles with different Gd^{3+} concentrations were synthesized by an eco-friendly microwave hydrothermal method. X-ray diffraction measurements confirm that the prepared nanoplates exhibit hexagonal wurtzite structure. Gd^{3+} doping induces lattice expansion of ZnO due to the larger ionic radius of rare earth Gd^{3+} in relation to Zn^{2+} ions. Rietveld refinement, Raman and Photoluminescence (PL) spectra confirm that Gd^{3+} ions were successfully inserted into ZnO lattice. The 2.0 mol% Gd^{3+} doped sample exhibits an increased photoluminescence intensity in comparison to that for the undoped ZnO, which is attributed to the enhance in the defect concentration due to Gd^{3+} doping. The photocatalytic activities of the samples were also evaluated towards UV-A induced degradation of methylene blue in aqueous solution. The highest photocatalytic activity was observed for 1.0 mol% Gd^{3+}-doped ZnO nanoparticles (73% for methylene blue degradation within 150 min under UV–Vis irradiation). The particles size, agglomeration degree and the electronic effects due to the Gd^{3+} dopping seems to be the main parameters that affect the photocatalytic activity of Gd^{3+}-doped ZnO nanoparticles.

Graphical abstract

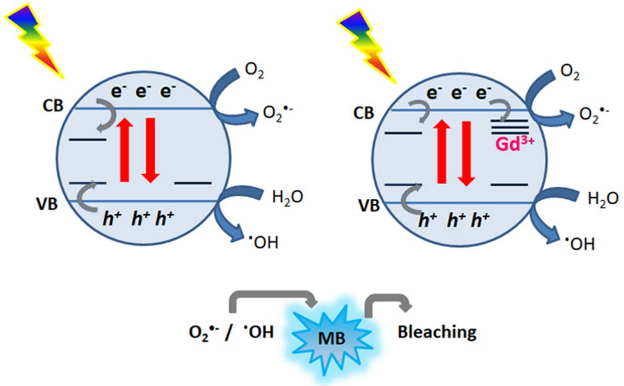

Keywords Zinc oxide · Rare earth · Nanoparticles · Photoluminescence · Photocatalysis

---

✉ Renata C. Lima, rclima@ufu.br; Juliane Z. Marinho, juliane_zacour@yahoo.com.br; Leonardo F. de Paula, leofpaula@hotmail.com; Elson Longo, elson.liec@gmail.com; Antonio O. T. Patrocinio, otaviopatrocinio@ufu.br | [1]Instituto de Química, Universidade Federal de Uberlândia, Uberlândia, MG 38400-902, Brazil. [2]LIEC, Departamento de Química, Universidade Federal de São Carlos, São Carlos, SP 13565-905, Brazil.

SN Applied Sciences (2019) 1:359 | https://doi.org/10.1007/s42452-019-0359-x

Received: 11 January 2019 / Accepted: 11 March 2019 / Published online: 25 March 2019

1 Introduction

Metal oxide semiconducting nanostructures doped with trivalent lanthanides ions (Ln^{3+}) are one of the most promising materials having most different applications in the field of light-emitting displays, magnetic recording media, photocatalysis and optical storage [1–4]. The optical emissions arising from the surface defect states of these semiconductors are effectively controlled by incorporating rare earth (RE) ions [1]. RE ions are considered to be the better luminescent centers because of their intra-shell transitions which can produce narrow and intense emission lines [1, 5]. The RE ions are incorporated into metal oxide semiconductors for the modification of electronic structure to improve optical, magnetic and catalytic properties [6–9].

One of the difficulties related with the synthesis of semiconductor nanoparticles is the control of growth by variation reaction parameters [10–13], such as concentration, temperature, pH, surfactant agent and synthesis time. These parameters directly influence the size and the morphology of nanoparticles. Furthermore, changing a synthetic strategy route can also introduce promising results. Microwave-hydrothermal (MH) method has attracted great attention as a heating process for semiconductor materials due to their kinetic advantages in comparison with the conventional hydrothermal method. As a modification of conventional hydrothermal, MH method is rapid volumetric heating without the heat conduction process, which can achieve uniform heating in a short period of time, and it can clearly decrease the reaction temperature of synthesis, obtain highly crystalline products with high purity and low aggregation morphologies, can also screen a wide range of experimental conditions in order to optimize the material properties [14–20]. Due to these advantages the microwave-hydrothermal method becomes a promising choice in the synthesis of nanostructured materials.

Among many oxides, zinc oxide (ZnO) is an important functional semiconducting material with a direct band gap of 3.37 eV, physical and chemical stability, weak cytotoxicity, high photosensitivity and piezoelectric properties [21, 22]. This has made ZnO a good candidate for technological application such as energy conversion, photocatalysis, sensors, LED’s and antibacterial properties [23–28]. Furthermore, ZnO has attracted attention for environmental remediation such as industrial wastewater treatment [29–31]. Under UV–Vis light irradiation, pollutant could be decomposed into non-toxic substances on the surface of a ZnO based photocatalyst [32–34]. However, the fast recombination of photogenerated electron–hole pairs is the main obstacle for increasing the photocatalytic efficiency of ZnO [35–37]. To enrich the photocatalytic, optical and magnetic properties of pure ZnO, many efforts have been made, as morphologies tuning, homogenous particles obtention and modification by doping with non-metals, alkali metals, transition metals (TM) as well as rare-earth (RE) metals [38–42]. Rare-earth metals doped ZnO nanostructures it’s a good alternative, which produced impurity energy levels in band gap and traps for photogenerated charges carriers accelerating the interfacial charge transfer and decreasing the recombination of electron–hole pairs [43, 44]. Gadolinium with half-filled f orbital has a mainly positive effect on the optical, electronic and magnetic properties when is used as a dopant for ZnO [42, 45]. Some researches for the beneficial effects of Gd on photocatalytic and optical properties of ZnO nanostructures but also, other semiconductors have been reported [46–49].

In this work, ZnO doped with 1.0 and 2.0 mol% Gd^{3+} were prepared by microwave-hydrothermal method. Crystalline and morphological homogeneous structures, optical and photocatalytic activity of synthesized nanoparticles were studied using different techniques.

2 Materials and methods

2.1 Preparation of Gd^{3+}-doped ZnO nanoplates

1.22×10^{-2} mol of $Zn(CH_3COO)_2{\cdot}2\,H_2O$ was added to 40 mL of distilled water. This solution was placed under constant stirring until complete dissolution of the salt. To this solution was added 1.0 mL of polyethylene glycol 400 (PEG 400). The pH value was raised to approximately 12 with the addition of a 2 mol L^{-1} KOH solution. Gd^{3+}-doped samples were obtained with the stoichiometric addition of the $Gd(NO_3)_3$ 0.28 mol L^{-1} (1.0 and 2.0 mol%) solution under constant stirring. The solutions were transferred to a polytetrafluoroethylene cup which was inserted into the reactor. The reaction system was heated to 90 °C for 16 min, with a heating rate of 5 °C min^{-1}. The pressure inside the autoclave was stabilized at 1.5 atm. The final products were centrifuged, washed repeatedly with distilled water and ethanol, and finally dried in an oven at 80 °C.

2.2 Characterization of the as-prepared samples

The X-ray diffraction (XRD) analyses were used to obtain information about the crystalline structure of the ZnO samples. The measurements were performed on Shimadzu X-ray diffraction (XRD) 6000 (Japan) equipped with CuK radiation ($\lambda = 1.5406$ Å) in the 2θ range from 10° to 100° with 0.02°/min scan increment and steps with a fixed-time of 2 s. The refinement of XRD diffraction results was performed using the Rietveld's profile analysis method [50, 51], with the General Structure Analysis System (GSAS) program suite [52], with EXPGUI interface [53]. Raman spectra were performed at room temperature with an Ocean Optics portable spectrometer equipped with λ = 785 nm laser, operating at 499 mW. The morphological characterization was performed using a scanning electron microscope model EVO MA 10 of Zeiss. X-ray (EDX) spectroscopy was performed on an Oxford Instruments, operating at 200 kV. UV–visible spectra of ZnO and Gd^{3+}-doped ZnO samples were obtained on a Cary5G spectrophotometer in the 200–800 nm regions. Photoluminescence (PL) spectra were recorded at room temperature by a thermal Jarrel-Ash Monospec27 monochromator and a Hamamatsu R446 photomultiplier ($\lambda_{exc} = 350.7$ nm). The adsorption of N_2 and the desorption isotherms at 77.35 K were measured on a Quantachrome TouchWin automatic surface analyzer version 1.1. Before analysis, the samples were degassed under vacuum at 90° C for 3 h. The surface area was calculated according to the BET method (Brunauer, Emmett and Teller) [54].

2.3 Photocatalytic activity

The photocatalytic performance of the as-prepared undoped ZnO and Gd^{3+}-doped samples was evaluated by the degradation of methylene blue (MB) under UV–Vis light irradiation. A xenon lamp (300 W) was employed light source. The light beam was passed through a KG1 filter to remove UVB and UVC photons, thus the photoreactor was illuminated with wavelengths between 320 and 800 nm. In a typical procedure, 0.16 mg catalyst was dispersed into 16 mL aqueous solution of MB (0.02 mmol L^{-1}) in a double wallet borosilicate reactor. After stirring in the dark for 60 min, the suspensions were placed under UV–Vis light irradiation. The reactor was kept at 25 °C by a water bath, the samples were collect at regular intervals, centrifuged to remove the excess of powders and then subjected to spectrophotometric analysis in the UV–Vis region (SHIMADZU 1650PC with 0.1 cm optical path quartz cuvette). The discoloration curves were plotted from the absorbance values at the maximum wavelength of 663 nm for aqueous solutions of methylene blue at pH close to neutrality. The percentage of discoloration was calculated by following the formula (Eq. 1):

$$\%\ \text{Decolorization} = \left[1 - \left(\frac{A_f}{A_i}\right)\right] \times 100 \qquad (1)$$

where A_f is the absorbance of the solution at time $t > 0$, and A_i is the initial absorbance of the solution. Photonic efficiency (ξ), which is defined as the ratio of the degradation rate of methylene blue (MB), r, and I the incident photon flux was also calculated as described elsewhere by using (Eq. 2) [55, 56]. The UV–Vis incident photon flux was determined by ferrioxalate actinometry [57] (9.20×10^{-8} Einstein s^{-1}).

$$\text{Photonic efficiency } (\xi) = \frac{r \times 100}{I} \qquad (2)$$

3 Results and discussion

XRD patterns refined by the Rietveld method are presented in Fig. 1a–c. Undoped ZnO and Gd^{3+}-doped samples present a single phase of wurtzite structure (JCPDS 36-1451), without the formation of secondary phases. Table 1 shows the Rietveld refinement indexes, the lattice parameters and volume, obtained by Rietveld refinement for undoped ZnO and Gd^{3+}-doped samples. The results were in good agreement with those observed and calculated XRD patterns. These results suggest that little fraction of Gd^{3+} are inserted into lattice or located as clusters on the surface of ZnO particles. It is known that the ionic radius of the Gd^{3+} and Zn^{2+} is 0.94 Å and 0.74 Å, respectively [45]. The wurtzite presents an open structure with interstices that can accommodate the Gd^{3+}, suggesting that rare-earth 3+ ions are replacing or displacing Zn^{2+} ions in the crystalline structure. Although differences of ionic radius, the replacing by Gd^{3+} ions do not cause changes in the crystalline wurtzite structure at long-range. In addition, the diffraction peak (101) of wurtzite phase get shifted towards the lower angle (Fig. 1d) which leads to an expansion of the unit cell and is due to the large ionic radius of rare earth Gd^{3+} than Zn^{2+} ions into ZnO sites [6, 45, 58]. This behavior is attributed to the substitution of Zn^{2+} by Gd^{3+} ions and therefore confirms the doping procedure. It means that ZnO lattice is expanded along the c-axis for Gd^{3+}-doped samples due to the mismatch between Gd^{3+} and ZnO of lattice in which ionic radii of Gd^{3+}, Zn^{2+} and O^{2-} is 0.94 Å, 0.74 Å and 1.32 Å, respectively [4, 59]. A slight expansion along a-axis was also observed. The increase for dopant promotes an increase in the number of defects in the crystalline lattice of the ZnO, thus leading to an increase in the lattice parameters.

The cell parameters (Table 1) indicate that doping with rare earth ions generates distortions in the crystalline lattice of ZnO and increases the amount of structural defects, such as oxygen and interstitial oxygen vacancies [43, 58, 60], since a slight increase was observed in the values of the cell parameters and consequently in an expansion of the unit cell when compared with the pure sample. This effect is consistent because the ions Gd^{3+} coordinate at

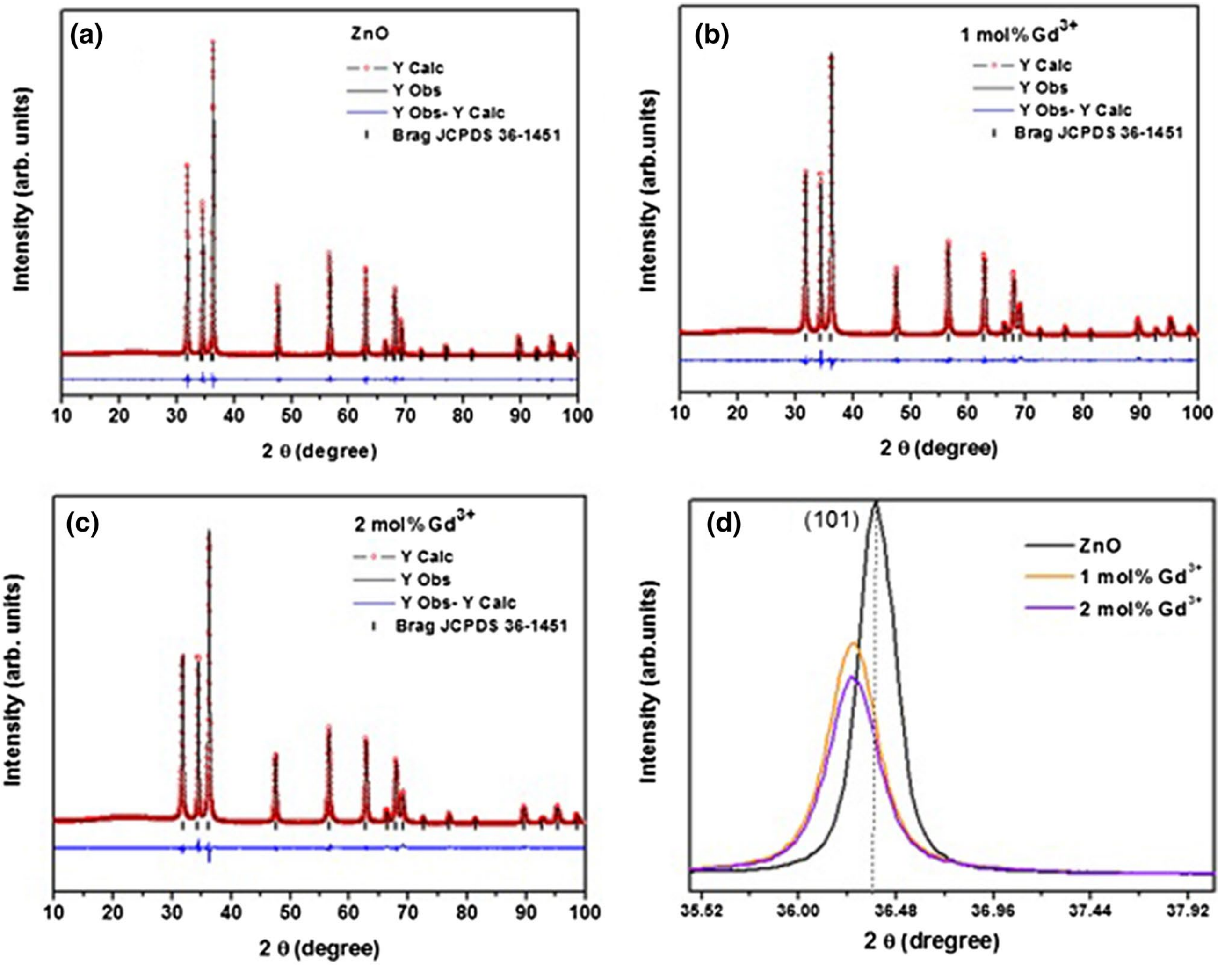

Fig. 1 Rietveld refinement plots for ZnO (**a**), 1.0 mol% of Gd^{3+} (**b**), 2.0 mol% of Gd^{3+} (**c**) and expanded region of the diffraction peak (101) (**d**)

Table 1 Parameters obtained from Rietveld refinement for ZnO, 1.0 mol% Gd^{3+} and 2.0 mol% of Gd^{3+} samples

Samples	Cell parameters			R_{wp} (%)	R_p (%)	R_{bragg} (%)	χ^2
	a = b (Å)	c (Å)	V (Å^3)				
ZnO	3.25014(5)	5.20715(9)	47.636(2)	4.86	3.68	1.59	1.65
1.0 mol% Gd^{3+}	3.25127(8)	5.20801(2)	47.677(3)	5.24	3.97	1.56	1.83
2.0 mol% Gd^{3+}	3.25132(9)	5.20871(3)	47.676(2)	4.94	3.74	1.82	1.63

octahedral positions preferentially in the crystalline lattice, occupying the interstitial sites [6].

Typical SEM images and EDX spectra of undoped ZnO and Gd^{3+}-doped ZnO nanostructures prepared by microwave-hydrothermal method are shown in Fig. 2. The SEM images of ZnO Gd^{3+}-doped ZnO samples reflect that have nearly similar particles morphology with varying agglomeration degree. Plate like morphology was observed for all samples. In addition, the SEM image of undoped ZnO sample shows irregular, slightly agglomerated plates with an average thickness of 45 nm, Fig. 2a. The particles display slightly larger particles size than Gd^{3+}-doped samples. Both Gd^{3+}-doped samples (Fig. 2b, c) showed formation of agglomerated plates with a smaller thickness (35 nm). EDX analysis confirmed the presence of Gd^{3+} in the samples (Fig. 2d). The silicon peak (Si) observed in the spectra is due of to substrate signal. No other peak related to impurities was detected in the spectra which further confirm that Gd^{3+}-doped ZnO samples were successfully synthesized.

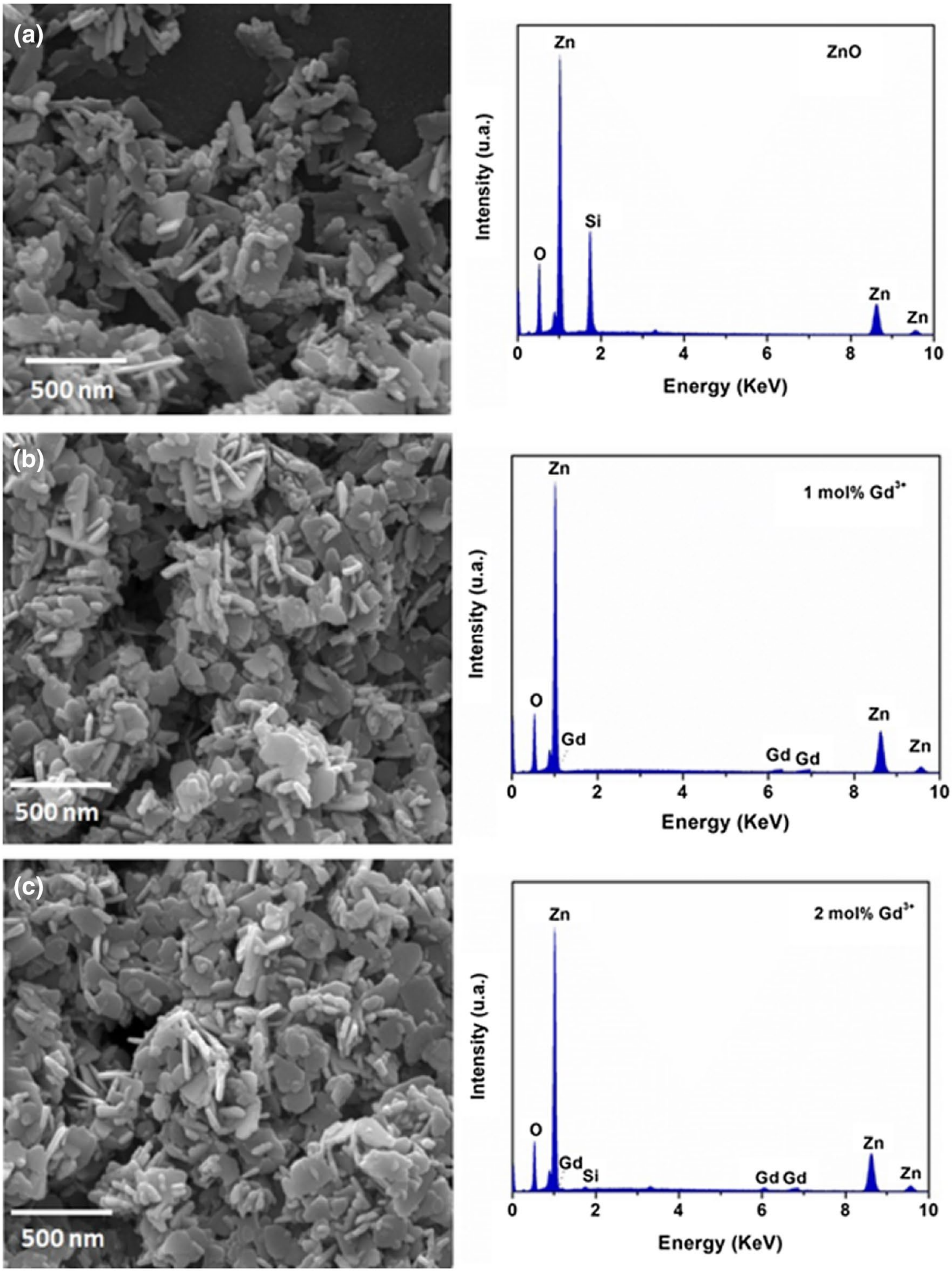

Fig. 2 SEM images of samples obtained by microwave hydrothermal method of ZnO (**a**), 1.0 mol% of Gd^{3+} (**b**) and 2.0 mol% of Gd^{3+} (**c**). The EDX spectra are on the right side of the micrographs

According to the literature, under conditions of thermodynamic equilibrium, the faster growth rate of ZnO is along the direction [0001] because of its higher surface energy and under certain physical chemical conditions, growth along this direction can be partially suppressed [61]. The formation of ZnO nanoplates or nanosheets may be associated with excess OH^- in the reaction medium allied to a prolongation of synthesis time (16 min). These external factors possibly retard the growth in the direction [0001], favoring the direction $[01\bar{1}0]$ in the formation and growth of the nanoplates [23].

The Raman spectra of ZnO and Gd^{3+}-doped ZnO powders are shown in Fig. 3. Wurtzite-type ZnO hexagonal symmetry belongs to the space group $P6_3mc$, with two formula units per primitive cell. Zinc oxide presents eight optical Raman mode sets (phonon modes) at the point of the Brillouin zone in the ZnO monocrystal, being described as follows by the representation: $\Gamma = A_1 + A_2 + B_1 + B_2 + 2\ E_1 + 2\ E_2$, where modes B_1 are silent, A_1 and E_1 are polar modes, active in both the Raman and the infrared, while E_2 modes are nonpolar active only in the Raman [62, 63].

The most intense mode in the Raman spectra is the E_{2H} at 438 cm^{-1}, characteristic of the wurtzite phase of ZnO, attributed to the zinc-oxygen vibration in the crystalline lattice [63, 64]. The slight asymmetries observed between samples are attributed to short-range structure disorder as well as to non-harmonic phonon–phonon interactions. As the concentration of the Gd^{3+} ions increases, a decrease in the intensity of the E_{2H} mode is observed, due to the distortions generated and consequently, a short-range structural disorder (Fig. 3b). The band located in the 210 cm^{-1} region refers to the $2E_{2L}$ mode of the second-order phonons. The low frequency bands around 334 cm^{-1} can be attributed to the second order Raman spectrum resulting from the E_{2H}–E_{2L} phonons. The polar phonons A_1 and E_1, as opposed to the E_2 phonons, are both divided into phonons TO and LO. The vibrational mode E_1 (LO) located in the region around 580 cm^{-1} rises from background, which originate from second-order Raman scattering, is associated with structural defects formed by oxygen vacancies [64, 65]. The low intensity band attributed to the order–disorder degree of ZnO A_1 (TO) around 378 cm^{-1} was observed to ZnO pure. The band at 409 cm^{-1} for the E_1 (TO) mode is observed as a "shoulder" of the band at 438 cm^{-1} (E_{2H}) and with the insertion of the dopant into ZnO crystal lattice it is covered by the E_{2H} mode (Fig. 3b). A narrow band referring to the intrinsic TA + LO mode of ZnO was observed around of 660 cm^{-1} [65, 66].

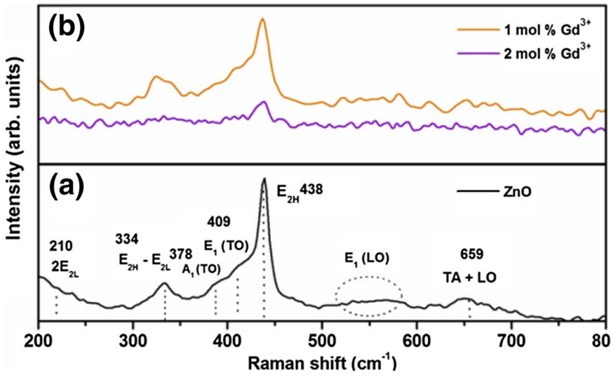

Fig. 3 The Raman spectra of ZnO (**a**), 1.0 mol% of Gd^{3+} and 2.0 mol% of Gd^{3+} (**b**) samples obtained by microwave hydrothermal method

In the literature, a similar behavior was observed, confirming that the influence of RE ion on the crystal structure arises from the strong dependence on the size and polarizability of the dopant ion [67]. The incorporation of Gd^{3+} ions promotes a tendency to electronic cloud distortion due to the increased polarization intensity. The Gd^{3+} presents a higher ionic radius and has the capacity to promote a distortion of the electronic cloud.

To investigate the specific area and the porosity of the ZnO and Gd^{3+}-doped ZnO nanoplates, Brunauer–Emmett–Teller (BET) adsorption and desorption of $N_2(g)$ measurements were performed. The nitrogen adsorption and desorption isotherms are shown in Fig. 4. All samples presented the type IV curve accompanied by a H3 type hysteresis, which is attributed to the predominance of mesopores according to the IUPAC classification [68, 69]. In addition, the BET surface area and pore distribution of all the samples are summarized in Table 2. The BET tests show that surface areas are 11.89 $m^2\ g^{-1}$, 13.94 $m^2\ g^{-1}$ and 7.84 $m^2\ g^{-1}$ for undoped ZnO, 1.0 mol% of Gd^{3+} and 2.0 mol% of Gd^{3+}, respectively. 1.0 mol% of Gd^{3+}-doped ZnO with a relatively higher specific surface possibly provides more active sites and is more beneficial for the photocatalytic reaction. Small particle sizes and minimized agglomeration increase the specific surface area and therefore also increase the number of active surface sites where the photogenerated charge carriers can react efficiently with absorbed molecules to form hydroxyl radicalar species [70, 71].

Variation in the specific surface area has been observed in the literature from insertion of dopants in the ZnO lattice. Liang et al. [32] synthesized Ce-doped ZnO microflowers at different concentrations (0.25–5.0% of Ce) and observed a decrease in the specific when the Ce^{4+} concentration was increased to 3.0%. Li et al. [72] obtained Er-doped ZnO samples via sol–gel method at concentration of 0.2%, 0.5% and 1.0% of Er. The authors reported that Er^{3+} concentrations were increased of 0 to 0.5%, the specific surface area increased, while the specific surface area decreased when the concentration increased to 1.0%.

The UV–visible diffuse reflectance spectra of the samples of pure zinc oxide and doped with the Gd^{3+} ions synthesized at 16 min times, are shown in Fig. 5. The Gd^{3+} ion with $4f^7$ configuration is very stable, *f*–*f* electronic transitions are difficult to detect, commonly is observed in the vacuum ultraviolet region (10–200 nm) [73]. To determine the gap energy (E_{gap}) values of the synthesized materials,

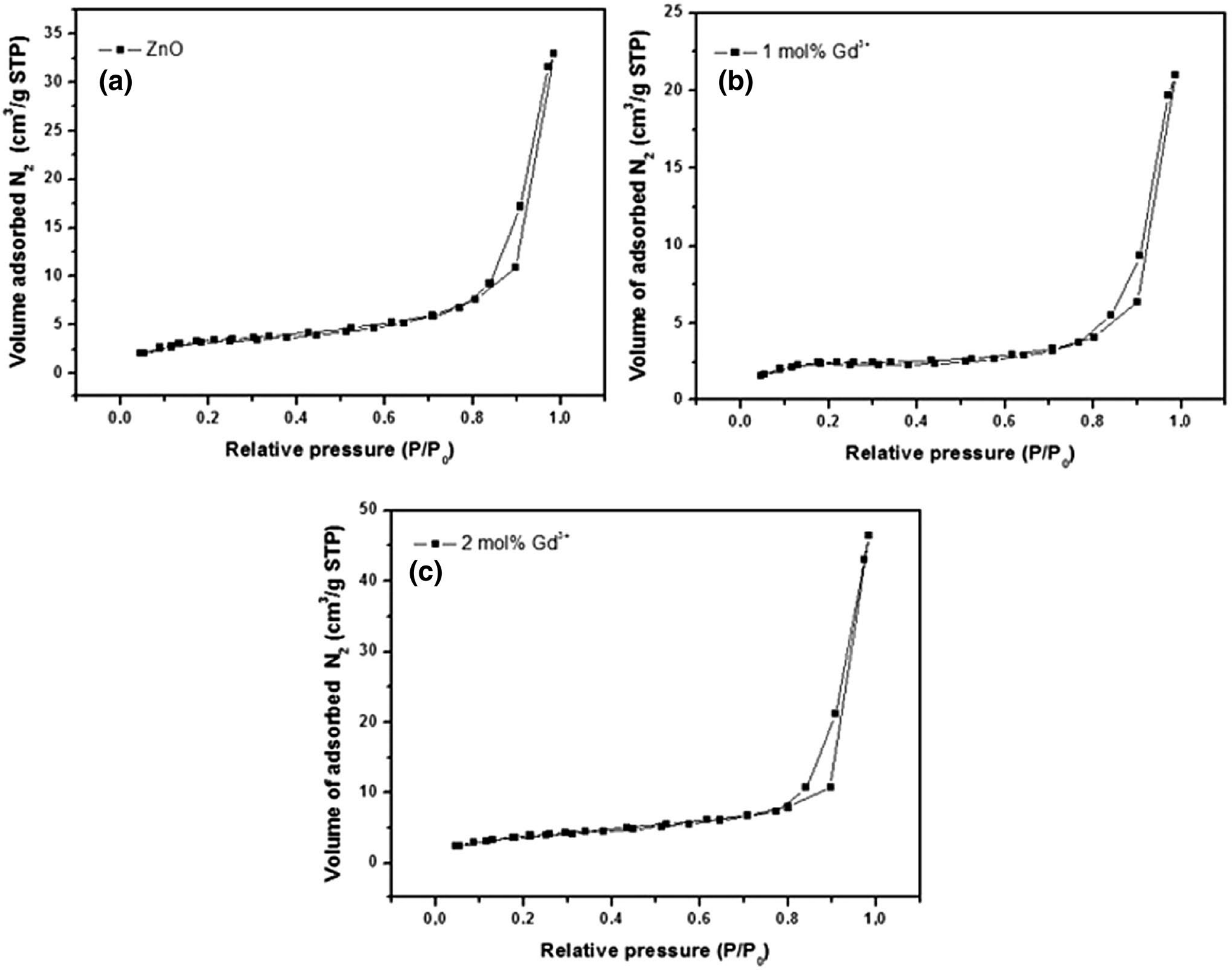

Fig. 4 N_2 adsorption/desorption isotherms of ZnO (**a**), 1.0 mol% of Gd^{3+} (**b**) and 2.0 mol% of Gd^{3+} (**c**) samples obtained by microwave hydrothermal method

Table 2 BET surface area of plate-like ZnO and Gd^{3+}-doped samples with different Gd^{3+} concentrations

Samples	Surface area (m^2 g^{-1})	Total pore volume (m^3 g^{-1})	Pore size (nm)
ZnO	11.89	0.051	17.18
1.0 mol% Gd^{3+}	13.94	0.072	16.60
2.0 mol% Gd^{3+}	7.84	0.033	2.06

the Kubelka–Munk method [74] was used. The E_{gap} values obtained were 3.28 eV; 3.25 eV and 3.26 eV, for samples of undoped ZnO, doped with 1 mol% Gd^{3+} and doped 2 mol% Gd^{3+}, respectively. The insertion of a dopant in the structure of the zinc oxide did not promote significant changes in the E_{gap} values of the materials, which is possibly due to the low concentrations of the doped ions Gd^{3+}

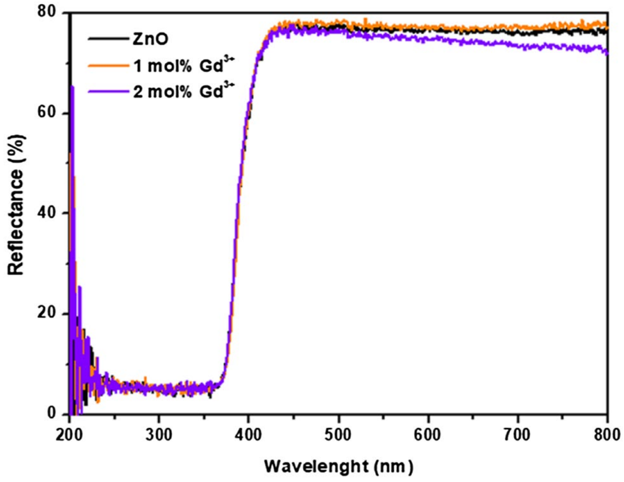

Fig. 5 UV–Vis diffuse reflectance spectra of nanoplates ZnO and doped with 1.0 and 2.0 mol% of Gd^{3+}

inserted in the crystalline lattice of ZnO. But also, the estimated E_{gap} experimental values were close to the theoretical E_{gap} value of ZnO (3.37 eV) [75, 76].

Photoluminescence spectra obtained at room temperature for samples of pure ZnO and doped with the Gd^{3+} ions synthesized at 16 min are shown in Fig. 6a. All samples presented a maximum broad band around 613 nm, which corresponds to the green and orange emission contributions. The photoluminescence intensity of 2.0 mol% of Gd^{3+} sample increased, suggesting that the recombination of the electrons and holes increases. This increase can be attributed to the surface defects of vacancies created by an increase in dopant concentration in the crystalline lattice, which act as centers of radiative recombination [32, 77]. The similar behavior was observed by Sowik et al. [78] that reported the modification of ZnO quantum dots with rare earth metals. The modification of ZnO with small amount of rare earth metal influenced lower PL intensity, however modification of ZnO by 0.18 or more mmol of La and Er caused increased in PL emission intensity.

It is widely accepted that the deep-level-emission is closely related to the structural defects such as oxygen vacancies or Zn interstitials in zinc oxide [4]. By using the Gaussian analysis, Fig. 6b–d shows the decomposition curves for the samples of undoped ZnO and doped with Gd^{3+} ion. From the results it was possible to attribute how much each color contributed to the photoluminescent emission. The bands were decomposed into five components, two components in the region of green (515 and 562 nm), one component in the region of orange (613 nm) and two components in the red region (665 and 736 nm). Table 3 shows the maximum peak values for each emission component and its percentage of area.

Doping can generate defects, which result in different recombination processes influencing emission in the visible region. As the dopant concentration increased in the

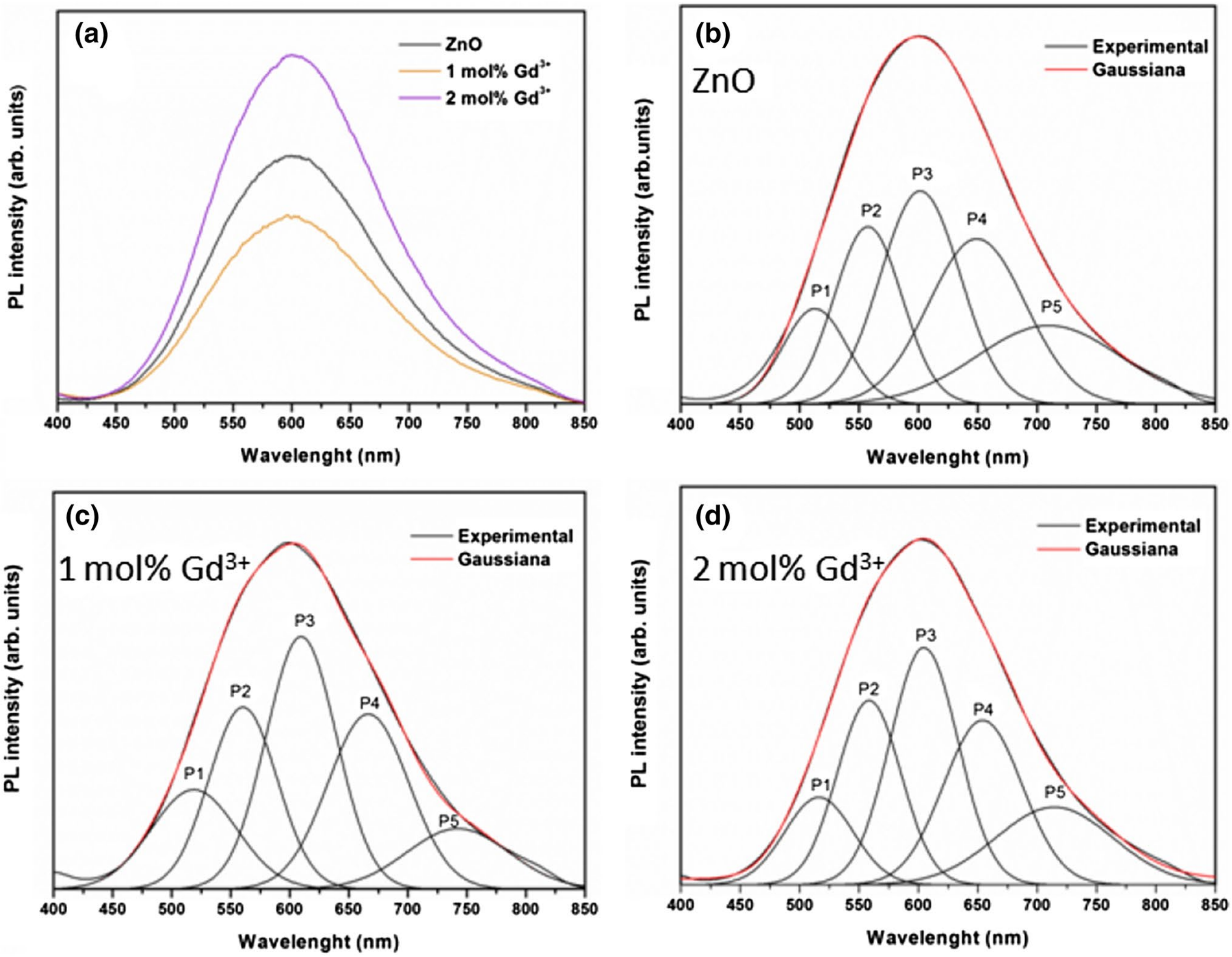

Fig. 6 **a** Photoluminescent emission spectra ($\lambda_{exc} = 350.7$ nm) for ZnO and Gd^{3+}-doped ZnO, **b** decomposition emission bands for the samples of undoped ZnO, **c** doped with 1.0 mol% of Gd^{3+} and **d** doped with 2.0 mol% of Gd^{3+}

Table 3 Relative percentage of the Gaussian deconvolution of the photoluminescence bands for the samples

PL peaks	Center (nm)	Samples		
		ZnO	1.0 mol% of Gd^{3+}	2.0 mol% of Gd^{3+}
		Area (%)		
P1 (green)	515	9.8	14.4	11
P2 (green)	562	19.2	21	23
P3 (orange)	613	27.1	30.1	29
P4 (red)	665	25.7	24	23.2
P5 (red)	736	18.2	10.5	13.8

ZnO crystal lattice, a higher percentage of green emission-related area can be observed by the contributions of the two peaks P1 and P2. The greater percentage of area in the green region correlate with the increase in the amount of dopant in the structure is attributed to the increase in the density of structural defects created, such as interstitial oxygen and zinc vacancies, as well as electronic defects [79–82]. Red emission bands can be attributed to free electron recombination and may be associated with excess oxygen occupying interstitial sites O_i [23, 83, 84]. The slight increase in emission in the orange-red regions from doping can be directly associated with the transitions of impurity levels induced by the presence of rare earth ion and also for changes in levels of impurities associated with native defects in ZnO.

The photocatalytic activity of the samples was evaluated against the degradation of the MB dye under UV–Vis irradiation. The degradation curve of MB without any catalyst added is also presented. As shown in Fig. 7a, there is a small decrease in the absorbance of MB in the blank experiment after 180 min of irradiation, indicating that the photolysis of MB solution resulted in degradation of 12%.

The 1.0 mol% of Gd^{3+}-doped ZnO nanoplates catalyst exhibit higher photocatalytic activity than those observed for the other samples (Fig. 7b), which corroborates with the PL behavior. The photocatalytic activity is affected by photo-generated charge transfer and separation, so the PL emission spectra can be used to estimate the separation capability of the electron–hole pairs. The PL emission is the result of the radiative recombination of electrons and holes. So, lower PL intensity reflects lower recombination yields of electron–hole pairs [7, 48]. Therefore, photocatalyst with weaker PL intensity tends to show higher catalytic ability.

The 1.0 mol% Gd^{3+}-doped ZnO shows lower emission intensity and consequently, its photocatalytic efficiency is higher when compared to the undoped ZnO. The introduction of Gd^{3+} ions can generates an increase in the number of structural defects in the crystalline ZnO lattice, as oxygen vacancies. The oxygen vacancies act as electron acceptors during photocatalytic process, which trap the photogenerated electrons temporally to reduce the recombination of electrons and holes, providing an alternative path [43, 85]. If the amount of rare earth ions exceeds the dopant acts as recombination center for electrons and holes, so the photocatalytic activity decreases, also observed in literature [48, 86].

Yi et al. [4] reported that the degradation rate of MB on Gd^{3+}-doped ZnO films with various Gd^{3+} contents under UV illumination. With increasing Gd^{3+} content, the photocatalytic activity of the Gd^{3+}-doped ZnO films decreases. This similar tendency is also observed for

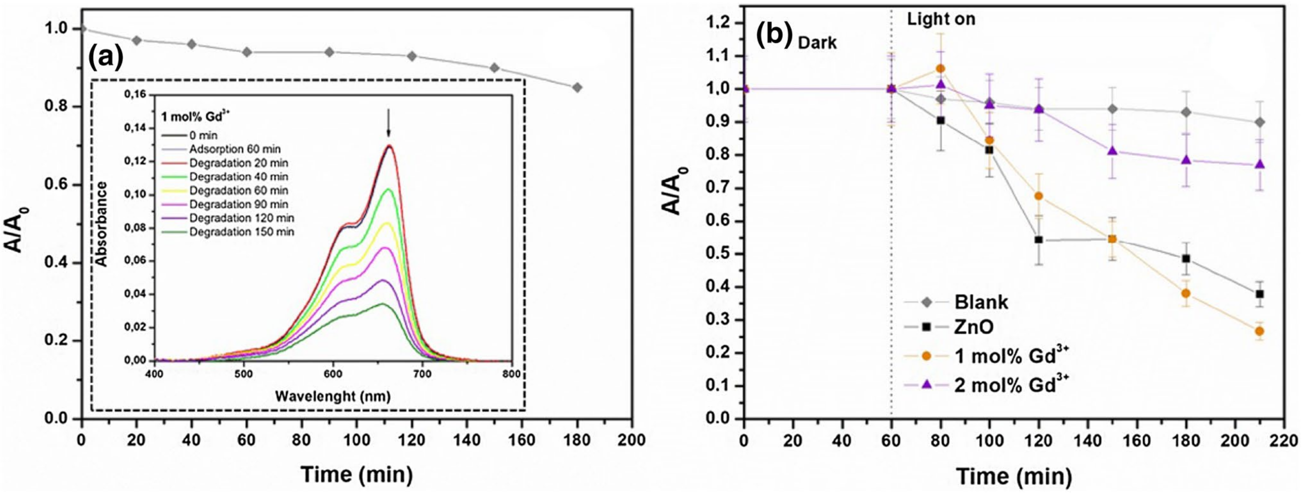

Fig. 7 **a** Photolysis of the methylene blue in the absence of the catalyst at a total time of 180 min and **b** photodegradation curves of MB by different catalysts under UV–Vis irradiation

Divya et al. [87]. They have prepared Gd^{3+}-doped ZnO varying the Gd^{3+} concentration between 0.05 and 0.2 wt%. The sample with 0.05 wt% Gd^{3+} has shown better photoactivity as compared to the other samples. Yayapao et al. [88] reported the degradation of MB under UV–Vis illumination in presence of Gd^{3+}-doped ZnO and also observed increased photoactivities for doped samples.

The photocatalytic degradation of methylene blue under UV–Vis irradiation is in accordance with the Langmuir–Hinschelwood model, which is well established in the literature [89–91]. Pseudo-first order rate constants (k) could be obtained by linear fittings of ln (A/A_0) versus the irradiation time, Fig. 8. A is the absorbance of the solution at time $t > 0$, and A_0 is the initial absorbance of the solution after the equilibration in the dark. The rate constants were calculated along with the percentage of methylene blue discoloration and the photonic efficiency (ξ), Table 4. The results confirmed the improvement of the photocatalytic activity of ZnO due to the doping with 1.0 mol% of Gd^{3+}.

The possible mechanism for describing the methylene blue photodegradation is illustrated in Fig. 9. The oxygen vacancies (V_0^+) and Gd^{3+} ion will act as electron acceptor, interstitial oxygen (O_i) will capture the holes, retarding the recombination of the charge carriers. New intermediate energy levels located between the valence band and the conduction band of ZnO are generated by the Gd^{3+} doping. The photoinduced holes react with adsorbed H_2O generating the oxygen radical species, responsible for the degradation of organic contaminants [7, 32, 43].

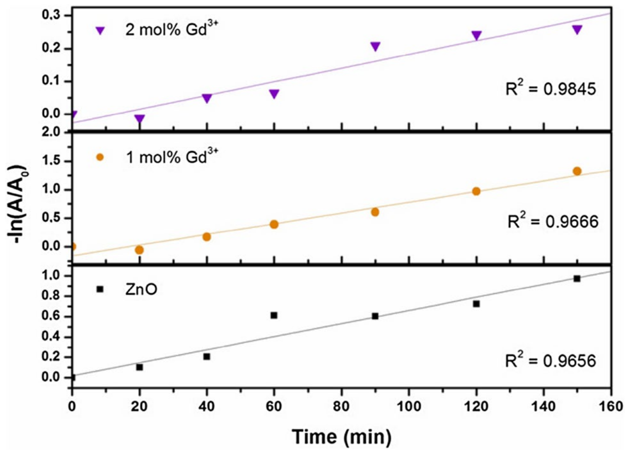

Fig. 8 Degradation of MB plotted as—ln (A/A_0) as a function of irradiation time using different catalysts, adjusted according to a pseudo-first order kinetics

Table 4 Observed rate constants (k), percentages of MB discoloration and photonic efficiencies (ξ) for different photocatalysts, under the irradiation conditions employed in this work (9.20×10^{-8} Einstein s^{-1})

Samples	Kinetic constant k (min^{-1})	Discoloration (%) after 150 min	Photonic efficiency (ξ) (%)
ZnO	0.0065	63	0.01
1.0 mol% Gd^{3+}	0.0093	73	0.02
2.0 mol% Gd^{3+}	0.0021	23	0.006

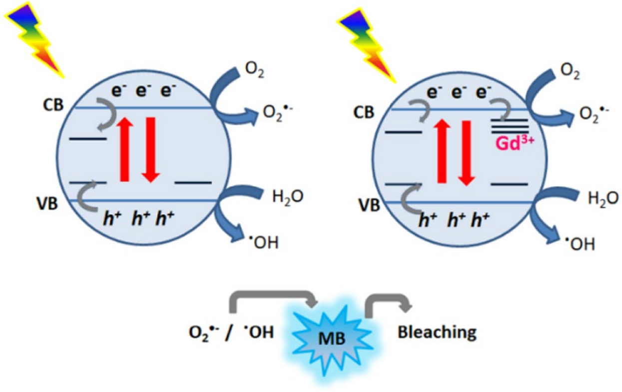

Fig. 9 Proposed scheme for the photodegradation of methylene blue under UV–Vis light irradiation

4 Conclusions

In summary, nanoplates of undoped ZnO an doped with Gd^{3+} ions were successfully synthetized using microwave hydrothermal method at only 90 °C for 16 min. XRD, Raman and photoluminescence confirmed the insertion of Gd^{3+} ions into ZnO crystal lattice. Are also investigated the influence of native defects of ZnO and Gd^{3+} ions on the photoluminescence and photocatalytic efficiency of the samples undoped ZnO an doped with Gd^{3+}. The BET surface measurements showed that 1 mol% of Gd^{3+} exhibited the higher surface area. All samples presented photocatalytic activity for the degradation of MB. Moreover, the sample doped with 1.0 mol% of Gd^{3+} presented highest photocatalytic activity. The results showed that the insertion of dopant Gd^{3+} increased the number of structural defects of the ZnO crystal lattice, therefore, the oxygen vacancies played a relevant role in the enhanced photocatalytic efficiency.

Acknowledgements Authors are grateful to Coordenação de Aperfeiçoamento de Pessoal de Nível Superior (Capes), Conselho Nacional de Desenvolvimento Científico e Tecnológico (CNPq), Fundação de Amparo à Pesquisa do Estado de Minas Gerais (FAPEMIG), Laboratório Multiusuário de Microscopia Eletrônica da Faculdade de Engenharia Química—UFU (FEQUI—UFU) and Rede Mineira de Química (RQ-MG). The authors are also thankful to the Grupo de Materiais Inorgânicos do Triângulo (GMIT), a research group supported by FAPEMIG (APQ00330-14).

Compliance with ethical standards

Conflict of interest The authors declare that they have no conflict of interest.

References

1. Sahu D, Panda NR, Acharya BS (2017) Effect of Gd doping on structure and photoluminescence properties of ZnO nanocrystals. Mater Res Express 4:114001–114009
2. Dramićanin MD (2016) Sensing temperature via downshifting emissions of lanthanide-doped metal oxides and salts. A review. Methods Appl Fluoresc 4:042001–042023
3. Mukherjee P, Shade CM, Yingling AM, Lamont DN, Waldeck DH, Petoud S (2011) Lanthanide sensitization in II–VI semiconductor materials: a case study with Terbium(III) and Europium(III) in zinc sulfide nanoparticles. J Phys Chem A 115:4031–4041
4. Yi XY, Ma CY, Yuan F, Wang N, Qin FW, Hu BC, Zhang QY (2017) Structural, morphological, photoluminescence and photocatalytic properties of Gd-doped ZnO films. Thin Solid Films 636:339–345
5. Murmu PP, Mendelsberg RJ, Kennedy J, Carder DA, Ruck BJ et al (2011) Structural and photoluminescence properties of Gd implanted ZnO single crystals. J Appl Phys 110:1–6
6. Aggarwal N, Kaur K, Vasishth A, Verma NK (2016) Structural, optical and magnetic properties of Gadolinium-doped ZnO nanoparticles. J Mater Sci Mater Electron 27:13006–13011
7. Khataee A, Soltani RDC, Karimi A, Joo SW (2015) Sonocatalytic degradation of a textile dye over Gd-doped ZnO nanoparticles synthesized through sonochemical process. Ultrason Sonochem 23:219–230
8. Apostolov AT, Apostolova IN, Wesselinowa JM (2018) Magnetic properties of rare earth doped SnO_2, TiO_2 and CeO_2 nanoparticles. Phys Status Solidi B 255:18001791–18001796
9. Paul S, Choudhury B, Choudhury A (2014) Magnetic property study of Gd doped TiO_2 nanoparticles. J Alloys Compd 601:201–206
10. Viswanatha R, Sapra S, Amenitsch H, Sartori B, Sarma DD (2007) Growth of semiconducting nanocrystals of CdS and ZnS. J Nanosci Nanotechnol 7:1726–1729
11. Wawrzynczyk D, Nyk M, Bednarkiewicz A, Strek W, Samoc M (2014) Morphology- and size-dependent spectroscopic properties of Eu^{3+}-doped Gd_2O_3 colloidal nanocrystals. J Nanopart Res 16:1–13
12. Xu H, Wang W, Zhu W (2006) Shape evolution and size-controllable synthesis of Cu_2O octahedra and their morphology-dependent photocatalytic properties. J Phys Chem B 110:13829–13834
13. Vagadia M, Ravalia A, Khachar U, Solanki PS, Doshi RR, Rayaprol S, Kuberkar DG (2011) Size and grain morphology dependent magnetic behaviour of Co-doped ZnO. Mater Res Bull 46:1933–1937
14. Komarneni S, Katsuki H (2002) Nanophase materials by a novel microwave-hydrothermal process. Pure Appl Chem 74:1537–1543
15. dos Santos ML, Lima RC, Riccardi CS, Tranquilin RL, Bueno PR, Varela JA, Longo E (2008) Preparation and characterization of ceria nanospheres by microwave-hydrothermal method. Mater Lett 62:4509–4511
16. Li D, Huang J-F, Cao L-Y, Li J-Y, Ou Yang H-B, Yao C-Y (2014) Microwave hydrothermal synthesis of Sr^{2+} doped ZnO crystallites with enhanced photocatalytic properties. Ceram Int 40:2647–2653
17. Mendes PG, Moreira ML, Tebcherani SM, Orlandi MO, Andres J et al (2012) SnO_2 nanocrystals synthesized by microwave-assisted hydrothermal method: towards a relationship between structural and optical properties. J Nanopart Res 14:750–757
18. Thankachan RM, Joy N, Abraham J, Kalarikkal N, Thomas S, Oluwafemi OS (2017) Enhanced photocatalytic performance of ZnO nanostructures produced via a quick microwave assisted route for the degradation of rhodamine in aqueous solution. Mater Res Bull 85:131–139
19. Hsieh S-H, Ting J-M (2018) Characterization and photocatalytic performance of ternary Cu-doped ZnO/Graphene materials. Appl Surf Sci 427:465–475
20. Meng L-Y, Wang B, Ma M-G, Lin K-L (2016) The progress of microwave-assisted hydrothermal method in the synthesis of functional nanomaterials. Mater Today Chem 1–2:63–83
21. Qi K, Yang J, Fu J, Wang G, Zhu L, Liu G, Zheng W (2013) Morphology-controllable ZnO rings: ionic liquid-assisted hydrothermal synthesis, growth mechanism and photoluminescence properties. CrystEngComm 15:6729–6735
22. Ozgur U, Alivov YI, Liu C, Teke A, Reshchikov MA et al (2005) A comprehensive review of ZnO materials and devices. J Appl Phys 98:041301. https://doi.org/10.1063/1.1992666
23. Akir S, Barras A, Coffinier Y, Bououdina M, Boukherroub R, Omrani AD (2016) Eco-friendly synthesis of ZnO nanoparticles with different morphologies and their visible light photocatalytic performance for the degradation of Rhodamine B. Ceram Int 42:10259–10265
24. Boujnah M, Boumdyan M, Naji S, Benyoussef A, El Kenz A, Loulidi M (2016) High efficiency of transmittance and electrical conductivity of V doped ZnO used in solar cells applications. J Alloys Compd 671:560–565
25. Ansari SG, Wahab R, Ansari ZA, Kim Y-S, Khang G, Al-Hajry A, Shin H-S (2009) Effect of nanostructure on the urea sensing properties of sol-gel synthesized ZnO. Sens Actuators B 137:566–573
26. Choi YS, Kang JW, Hwang DK, Park SJ (2010) Recent advances in ZnO-based light-emitting diodes. IEEE Trans Electron Devices 57:26–41
27. Qi K, Cheng B, Yu J, Ho W (2017) Review on the improvement of the photocatalytic and antibacterial activities of ZnO. J Alloys Compd 727:792–820
28. Zheng P, Zhang B, Jin B, Guan W, Bai B, Dai S (2018) Synergistic enhancement in antibacterial activity of core/shell/shell SiO_2/ZnO/Ag_3PO_4 nanoparticles. ChemNanoMat 4:972–981
29. Umar A, Chauhan MS, Chauhan S, Kumar R, Kumar G et al (2011) Large-scale synthesis of ZnO balls made of fluffy thin nanosheets by simple solution process: structural, optical and photocatalytic properties. J Colloid Interface Sci 363:521–528
30. Zheng X, Wu R, Chen Y (2011) Effects of ZnO Nanoparticles on wastewater biological nitrogen and phosphorus removal. Environ Sci Technol 45:2826–2832
31. da Silva GTST, Carvalho KTG, Lopes OF, Gomes ES et al (2017) Synthesis of ZnO nanoparticles assisted by N sources and their application in the photodegradation of organic contaminants. ChemCatChem 9:3795–3804
32. Liang Y, Guo N, Li L, Li R, Ji G, Gan S (2015) Preparation of porous 3D Ce-doped ZnO microflowers with enhanced photocatalytic performance. RSC Adv 5:59887–59894
33. Jaramillo-Páeza C, Sánchez-Cida P, Navío JA, Hidalgo MC (2018) A comparative assessment of the UV-photocatalytic activities

of ZnO synthesized by different routes. J Environ Chem Eng 6:7161–7171
34. Moussa H, Chouchene B, Gries T, Balan L, Mozet K, Medjahdi G, Schneider R (2018) Growth of ZnO nanorods on graphitic carbon nitride gCN sheets for the preparation of photocatalysts with high visible-light activity. ChemCatChem 10:4973–4983
35. Liang Y, Guo N, Li L, Li R, Ji G, Gan S (2015) Fabrication of porous 3D flower-like Ag/ZnO heterostructure composites with enhanced photocatalytic performance. Appl Surf Sci 332:32–39
36. Kumar SG, Rao KSRK (2017) Comparison of modification strategies towards enhanced chargecarrier separation and photocatalytic degradation activity of metal oxide semiconductors (TiO_2, WO_3 and ZnO). App Surf Sci 391:124–148
37. Yu W, Zhang J, Peng T (2016) New insight into the enhanced photocatalytic activity of N-, C- and S-doped ZnO photocatalysts. Appl Catal B 181:220–227
38. Liu Y, Liu H, Zhou H, Li T, Zhang L (2019) A Z-scheme mechanism of N-ZnO/g-C_3N_4 for enhanced H_2 evolution and photocatalytic degradation. Appl Surf Sci 466:133–140
39. Ravichandran K, Chidhambaram N, Arun T, Velmathid S, Gobalakrishnan S (2016) Realizing cost-effective ZnO: Sr nanoparticles@graphene nanospreads for improved photocatalytic and antibacterial activities. RSC Adv 6:67575–67585
40. Kumar S, Song TK, Gautam S, Chae KH, Kim SS, Jang KW (2015) Structural, magnetic and electronic structure properties of Co doped ZnO nanoparticles. Mater Res Bull 66:76–82
41. Isik M, Gasanly NM (2019) Gd-doped ZnO nanoparticles: synthesis, structural and thermoluminescence properties. J Lumin 207:220–225
42. Yakout SM (2018) Pure and Gd-based Li, Na, Mn or Fe codoped ZnO nanoparticles: insights into the magnetic and photocatalytic properties. Solid State Sci 83:207–217
43. Thangaraj P, Viswanathan MR, Balasubramanian K, Panneerselvam S, Mansilla HD et al (2015) Morphology controlled synthesis of Sm doped ZnO nanostructures for photodegradation studies of Acid Blue 113 under UV-A light. J Mater Sci Mater Electron 26:8784–8792
44. Rezaei M, Habibi-Yangjeh A (2013) Microwave-assisted preparation of Ce-doped ZnO nanostructures as an efficient photocatalyst. Mater Lett 110:53–56
45. Vijayaprasath G, Murugan R, Hayakawa Y, Ravi G (2016) Optical and magnetic studies on Gd doped ZnO nanoparticles synthesized by co-precipitation method. J Lumin 178:375–383
46. Kumar S, Sahare PD (2014) Gd^{3+} incorporated ZnO nanoparticles: a versatile material. Mater Res Bull 51:217–223
47. Xu H, Wu C, Li H, Chu J, Sun G, Xu Y, Yan Y (2009) Synthesis, characterization and photocatalytic activities of rare earth-loaded $BiVO_4$ catalysts. Appl Surf Sci 256:597–602
48. Mishra P, Singh YP, Nagaswarupa HP, Sharma SC, Vidya YS et al (2016) Caralluma fimbriata extract induced green synthesis, structural, optical and photocatalytic properties of ZnO nanostructure modified with Gd. J Alloys Compd 685:656–669
49. Zhang N, Chen D, Niu F, Wang S, Qin L, Huang Y (2016) Enhanced visible light photocatalytic activity of Gd-doped $BiFeO_3$ nanoparticles and mechanism insight. Sci Rep 6:264671–2646711
50. Rietveld H (1969) A profile refinement method for nuclear and magnetic structures. J Appl Crystallogr 2:65–71
51. Sakata M, Cooper MJ (1979) An analysis of the Rietveld refinement method. J Appl Crystallogr 12:554–563
52. Larson AC and Dreele RBV (2000) General Structure Analysis System (GSAS) in L.A.N.L.R. LAUR ed, pp 86-748
53. Toby B (2001) EXPGUI, a graphical user interface for GSAS. J Appl Crystallogr 34:210–213
54. Brunauer S, Emmett PH, Teller E (1938) Adsorption of Gases in multimolecular layers. J Am Chem Soc 6:309–319
55. Serpone N, Terzian R, Lawless D, Kennepohl P, Sauve G (1993) On the usage of turnover numbers and quantum yields in heterogeneous photocatalysis. J Photochem Photobiol A Chem 73:11–16
56. Patrocinio AOT, Paula LF, Paniago RM, Freitag J, Bahnemann DW (2014) Layer-by-Layer TiO_2/WO_3 thin films as efficient photocatalytic self-cleaning surfaces. ACS Appl Mater Interfaces 6:16859–16866
57. Hatchard CG, Parker CA (1956) A new sensitive chemical actinometer II. Potassium ferrioxalate as a standard chemical actinometer. Proc R Soc Lond Ser A Math Phys Sci 235:518–536
58. Kaur P, Kumar S, Chen CL, Hsu YY et al (2016) Investigations on structural, magnetic and electronic structure of Gd-doped ZnO nanostructures synthesized using sol-gel technique. Appl Phys A 122:161–169
59. Ma X, Wang Z (2012) The optical properties of rare earth Gd doped ZnO nanocrystals. Mater Sci Semicond Process 15:227–231
60. Suwanboon S, Amornpitoksuk P, Sukolrat A, Muensit N (2013) Optical and photocatalytic properties of La-doped ZnO nanoparticles prepared via precipitation and mechanical milling method. Ceram Int 39:2811–2819
61. Dakhlaoui A, Jendoubi M, Smiri LS, Kanaev A, Jouini N (2009) Synthesis, characterization and optical properties of ZnO nanoparticles with controlled size and morphology. J Cryst Growth 311:3989–3996
62. Sharma D, Sharma S, Kaith BS, Rajput J, Kaur M (2011) Synthesis of ZnO nanoparticles using surfactant free in-air and microwave method. Appl Surf Sci 257:9661–9672
63. Ojha AK, Srivastava M, Kumar S, Hassanein R, Singh J, Singh MK, Materny A (2014) Influence of crystal size on the electron–phonon coupling in ZnO nanocrystals investigated by Raman spectroscopy. Vib Spectrosc 72:90–96
64. Lima RC, Macario LR, Espinosa JWM, Longo VM, Erlo R et al (2008) Toward an understanding of intermediate- and short-range defects in ZnO single crystals. A combined experimental and theoretical study. J Phys Chem A 112:8970–8978
65. Šćepanović M, Grujić-Brojčin M, Vojisavljević K, Bernik S, Srećković T (2010) Raman study of structural disorder in ZnO nanopowders. J Raman Spectrosc 41:914–921
66. Damen TC, Porto SPS, Tell B (1966) Raman effect in zinc oxide. Phys Rev 142:570–574
67. Wang F, Han Y, Lim CS, Lu Y, Wang J, Xu J et al (2010) Simultaneous phase and size control of upconversion nanocrystals through lanthanide doping. Nature 463:1061–1065
68. Kruk M, Jaroniec M (2001) Gas adsorption characterization of ordered organic-inorganic nanocomposite materials. Chem Mater 13:3169–3183
69. Yingying L, Leshu Y, Heyong H, Yuying F, Dongzhen C, Xin X (2012) Application of the soluble salt-assisted route to scalable synthesis of ZnO nanopowder with repeated photocatalytic activity. Nanotechnology 23:0654021–0654028
70. Almquist CB, Biswas P (2002) Role of synthesis method and particle size of nanostructured TiO_2 on its photoactivity. J Catal 212:145–156
71. Dodd AC, McKinley AJ, Saunders M, Tsuzuki T (2006) Effect of particle size on the photocatalytic activity of nanoparticulate zinc oxide. J Nanopart Res 8:43–51
72. Li C, Yan Z, Zhou Y, Zhao S, Zhang X, Sheng X (2018) Sol–gel synthesis of erbium-doped ZnO with nest structure for photocatalysis. Funct Mater Lett 11:17500821–17500824
73. Tsuboi T (1998) Absorption spectra due to the $4f^7 \rightarrow 4f^7$ transitions of Gd^{3+} ions in $GdAl_3(BO_3)_4$ crystals. J Phys Condens Matter 10:9155–9159
74. Patterson EM, Shelden CE, Stockton BH (1977) Kubelka–Munk optical-properties of a barium-sulfate white reflectante standard. Appl Opt 16:729–732

75. Janotti A, Van de Walle CG (2007) Native point defects in ZnO. Phys Rev B 76:1652021–16520222
76. Haffad S, Cicero G, Samah M (2011) Structural and electronic properties of ZnO nanowires: a theoretical study. Energy Procedia 10:128–137
77. Farooqi MMH, Srivastava RK (2016) Enhanced UV-vis photoconductivity and photoluminescence by doping of samarium in ZnO nanostructures synthesized by solid state reaction method. Optik 127:3991–3998
78. Sowik J, Miodyńska M, Bajorowicz B, Mikolajczyk A et al (2019) Optical and photocatalytic properties of rare earth metal-modified ZnO quantum dots. Appl Surf Sci 464:651–663
79. de Moura AP, Lima RC, Moreira ML, Volanti DP et al (2010) ZnO architectures synthesized by a microwave-assisted hydrothermal method and their photoluminescence properties. Solid State Ionics 181:775–780
80. Vanheusden K, Seager CH, Warren WL, Tallant DR, Voigt JA (1996) Correlation between photoluminescence and oxygen vacancies in ZnO phosphors. Appl Phys Lett 68:403–405
81. dos Reis PM, de Oliveira AS, Pecoraro E, Ribeiro SJL, Goes MS et al (2015) Photoluminescent and structural properties of ZnO containing Eu^{3+} using PEG as precursor. J Lumin 167:197–203
82. Flemban TH, Sequeira MC, Zhang Z, Venkatesh S, Alves E et al (2016) Identifying the influence of the intrinsic defects in Gd-doped ZnO thin-films. J Appl Phys 119:065301–065307
83. Biswas P, Baek S-D, Hoon Lee S, Park J-H, Jeong Lee S et al (2015) Low temperature solution process-based defect-induced orange-red light emitting diode. Sci Rep 5:1–8
84. Sanjaya B, Jayakrishna K, Sunkara S, Lo KY, Shivashankar SA (2015) Self-assembled ZnO nanoparticles on ZnO microsheet: ultrafast synthesis and tunable photoluminescence properties. J Phys D Appl Phys 48:225305-1–225305-12
85. Pan X, Yang M-Q, Xu Y-J (2014) Morphology control, defect engineering and photoactivity tuning of ZnO crystals by graphene oxide—a unique 2D macromolecular surfactant. Phys Chem Chem Phys 16:5589–5599
86. Chang C-J, Lin C-Y, Hsu M-H (2014) Enhanced photocatalytic activity of Ce-doped ZnO nanorods under UV and visible light. J Taiwan Inst Chem E 45:1954–1963
87. Divya NK, Pradyumnan PP (2017) High dielectric constant, low loss and high photocatalytic activity in Gd doped ZnO systems. Mater Res Express 4(015904):1–9
88. Yayapao O, Thongtem T, Phuruangrat A, Thongtem S (2015) Synthesis and characterization of highly efficient Gd doped ZnO photocatalyst irradiated with ultravioleta and visible radiations. Mater Sci Semicond Process 39:786–792
89. Chakrabarti S, Dutta BK (2004) Photocatalytic degradation of model textile dyes in wastewater using ZnO as semiconductor catalyst. J Hazard Mater 112:269–278
90. Yang H, Li GY, An TC, Gao YP, Fu JM (2010) Photocatalytic degradation kinetics and mechanism of environmental pharmaceuticals in aqueous suspension of TiO_2: a case of sulfa drugs. Catal Today 153:200–207
91. Oliveira DFM, Batista PS, Muller PS Jr, Velani V, França MD, de Souza DR, Machado AEH (2012) Evaluating the effectiveness of photocatalyts based on titanium dioxide in the degradation of the dye Ponceau 4R. Dyes Pigm 92:563–572